



Electrochemical reactions of AgFeO_2 as negative electrode in Li- and Na-ion batteries



Pedro Berastegui^a, Cheuk-Wai Tai^b, Mario Valvo^{a,*}

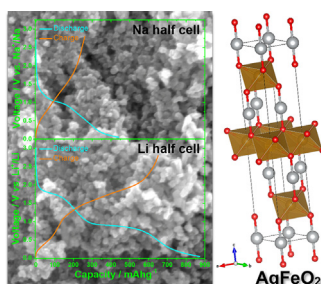
^a Department of Chemistry, Ångström Laboratory, Uppsala University, Box 538, 75121, Uppsala, Sweden

^b Department of Materials and Environmental Chemistry, Arrhenius Laboratory, Stockholm University, SE-10691, Stockholm, Sweden

HIGHLIGHTS

- Silver ferrite nanoparticles are produced via a simple, room-temperature synthesis.
- AgFeO_2 nanoparticles are studied as negative electrodes Li- and Na-ion batteries.
- AgFeO_2 forms Ag^0 nanoparticles upon reduction with Li^+ and Na^+ ions.
- AgFeO_2 reacts through combined conversion and alloying mechanisms.

GRAPHICAL ABSTRACT



ARTICLE INFO

Keywords:

Silver ferrite
Li- and Na-ion batteries
Negative electrodes
Conversion reactions
Electrochemical alloying
Metallic nanoparticles

ABSTRACT

AgFeO_2 nanoparticles synthesized via precipitation at room temperature are investigated in Li- and Na-ion cells through electrode coatings with an alginate binder. The electrochemical reactions of AgFeO_2 with Li^+ and Na^+ ions, as well as its role as alternative negative electrode in these cell systems are carefully evaluated. Initial Li uptake causes irreversible amorphization of the AgFeO_2 structure with concomitant formation of Ag^0 nanoparticles. Further Li incorporation results in conversion into Fe^0 nanoparticles and Li_2O , together with Li-alloying of these Ag^0 clusters. Similar mechanisms are also found upon Na uptake, although such processes are hindered by overpotentials, the capacity and reversibility of the reactions with Na^+ ions being not comparable with those of their Li^+ counterparts. The behaviour of AgFeO_2 at low potentials vs. Li^+/Li displays a synergic pseudo-capacitive charge storage overlapping Li-Ag alloying/de-alloying. This feature is exploited in full cells having deeply lithiated AgFeO_2 and LiFePO_4 as negative and positive electrodes, respectively. These environmentally friendly iron-based full cells exhibit attractive cycle performances with $\approx 80\%$ capacity retention after 1000 cycles without any electrolyte additive, average round trip efficiency of $\approx 89\%$ and operational voltage of 3.0 V combined with built-in pseudo-capacitive characteristics that enable high cycling rates up to $\approx 25\text{C}$.

1. Introduction

Electrochemical energy storage via rechargeable batteries is going to face a tantalizing challenge that goes beyond a sheer enhancement of their performances and necessarily involves crucial aspects regarding

their environmental footprint [1] and current use of critical materials [2,3]. This certainly applies to Li-ion batteries (LIBs), despite their tremendous success as dedicated power source in portable electronics, as the prospects of employing these cells in large-scale applications (e.g. electric vehicles, electrical grids) represent a serious concern in terms of

* Corresponding author.

E-mail address: mario.valvo@kemi.uu.se (M. Valvo).

<https://doi.org/10.1016/j.jpowsour.2018.09.002>

Received 13 June 2018; Received in revised form 27 August 2018; Accepted 2 September 2018

0378-7753/© 2018 The Authors. Published by Elsevier B.V. This is an open access article under the CC BY-NC-ND license (<http://creativecommons.org/licenses/by-nc-nd/4.0/>).

cost and environmental issues. The majority of LIB materials (e.g. electrodes, solvents, electrolytes) are hazardous, toxic and increasingly expensive (e.g. LiCoO₂, graphite), while their production and ultimate assembly in cells require a high energy expenditure that translates into significant gas emissions and pollution [4]. The scarce level of recycling of LIB components further complicates this scenario posing severe threats to the environment. Current debates about worldwide availability of lithium sources have also re-ignited interest in studying complementary Na-ion batteries (NIBs), which employ cheaper and more abundant sodium ores [5,6]. Irrespectively of the type of chemistry (e.g. Li⁺, Na⁺, K⁺, etc.) chosen for the electrochemical reactions in these rechargeable batteries, a critical role in terms of sustainability for the resulting cells is expected to be played mainly by the remaining elements or compounds constituting their electrode frameworks, where the ions are stored.

Transition metal oxides (TMOs) are particularly attractive for this purpose, as they can provide suitable hosts for these cations, convenient ranges of operation potentials and electrical conductivities, together with the key possibility of using abundant and benign elements (e.g. iron, manganese), which can favour a more cost-effective and less polluting battery production on a large scale.

Among several metal oxide compounds, a family of ternary oxides referred to as Delafossites has not been explored extensively in LIBs and NIBs so far. Delafossite-type oxides possess a characteristic layered structure with the general formula ABO₂, where A typically represents a monovalent metal cation (e.g. Ag⁺, Pt⁺, Cu⁺, etc.) that alternates with edge-sharing BO₆ octahedra (with B=Fe³⁺, Ni³⁺ or other trivalent metal cations) that are oriented orthogonally with respect to the c axis of the crystal lattice. A Delafossite structure can give rise to two different polytypes [7,8], namely 3R (rhombohedral) and 2H (hexagonal), depending on the orientation of each layer, with associated space group symmetries of *R*3̄*m* and *P*6₃/*mmc*, respectively.

To date, relatively few reports exist about Delafossite-type materials as alternative electrodes in LIBs (e.g. AgCuO₂ and AgCu_{0.5}Mn_{0.5}O₂ [9], CuFeO₂ [10–12], CuCrO₂ [13], AgFeO₂ [14] and Ag_xFeO_y composites [15–17]), while none for possible use of these compounds in analogous NIB applications, to the best of our knowledge.

Silver ferrite has received some attention in LIB investigations, thanks to its ease of synthesis at low temperatures [14,17] and good control of Ag/Fe ratios to produce different Ag_xFeO_y compositions [15,16] that deviate from a stoichiometric AgFeO₂ compound. AgFeO₂ and related variants have been investigated only as possible positive electrodes for LIBs so far. No information can be retrieved about its electrochemical properties as negative electrode in LIBs, apart from a recent synchrotron study that analysed only its first discharge from 3.0 V to 0.3 V vs. Li⁺/Li through in situ nano-fluorescence mapping [18]. In earlier studies, it was demonstrated that the layered structure of AgFeO₂ undergoes a structural change around 1.7 V vs. Li⁺/Li during initial insertion of Li⁺ ions due to an irreversible reduction of the Ag⁺ cations and the formation of Ag⁰ nanoparticles [14]. However, AgFeO₂ suffers mainly from three drawbacks as positive electrode, namely: *i.* it does not contain a Li⁺ source in its structure, thereby requiring additional (pre)lithiation, *ii.* irreversible structural changes caused by the Ag⁺ → Ag⁰ reduction negatively affect its insertion framework, this being reflected in a clear voltage hysteresis for the charge/discharge curves (i.e. higher energy losses), which become more sloping and steeper after the first discharge and *iii.* significant irreversible capacity loss occurs due to incomplete Ag oxidation upon initial charge [14,18]. Nevertheless, a capacity enhancement was also gained via a concomitant reduction of Fe³⁺ to Fe²⁺ accompanied by a massive resistivity decrease for these electrodes. The latter was due to finely dispersed silver nanoparticles when AgFeO₂ was subjected to a depth of discharge of two electron equivalents [14]. Hence, it is interesting to exploit these favourable features upon reaction with Li⁺ and to extend the AgFeO₂ operation domain towards lower voltages vs. Li⁺/Li. Indeed, higher capacities should be available through combined oxide

conversion [19–21] and Li-alloying [22–24] of its FeO₆ units and Ag⁰ nanoparticles, respectively. Bridging these storage mechanisms is also desirable to enhance electrode functionalities and promote synergic effects [25]. *In situ*-formed silver nanoparticles can play a crucial role, providing important benefits for these negative electrodes, as Ag offers the lowest resistivity (i.e. 1.59 μΩ cm at 20 °C). It should be possible then to achieve an excellent electronically conductive network [26,27] during the conversion of the FeO₆ units, in which highly resistive phases (i.e. Li₂O) are nucleated together with small Fe⁰ nanoparticles. A simultaneous, additional Li storage at low potentials via reversible formation of Li-Ag alloys [24,28,29] should be accessible as well.

With these ideas in mind, we report for the first time a detailed study of the electrochemical behaviour of AgFeO₂ as negative electrode in LIBs and some preliminary results for this compound in NIBs, too. It is shown that silver ferrite is apt to undergo electrochemical reactions at low potentials vs. both Li⁺ and Na⁺ ions in composite electrode coatings with a Na-alginate binder [30] and that the afore-mentioned mechanisms of conversion and alloying are substantially different in these two cases. A preliminary example of full Li-ion cell including prelithiated AgFeO₂ as negative electrode and LiFePO₄ as positive counterpart is presented as well.

2. Experimental

2.1. Material synthesis

Silver ferrite nanoparticles were prepared by a co-precipitation method employing silver nitrate (Fluka, > 99%) and iron (III) nitrate (Sigma-Aldrich, > 98%) as precursors and sodium hydroxide (Merck, > 98%) as reagent, respectively. 5 mmol of each nitrate were dissolved in 10 ml of deionized water while stirring and their respective solutions were mixed together at room temperature. A 2 M NaOH solution was then added dropwise while stirring to obtain a fine precipitate of silver ferrite nanoparticles. In order to ensure a complete precipitation, 15 ml of this solution were used. After allowing sedimentation, the solution was decanted and the precipitate centrifuged and washed five times. The powder was then air-dried overnight in an oven at 95 °C.

2.2. Materials characterization and electrochemical measurements

X-ray diffraction (XRD) was carried out on a Bruker D8 Advance diffractometer equipped with a LYNXEYE-XE detector set to minimize fluorescence using Cu Kα radiation in the 2θ range 10–90° with 0.02°/step. Scanning electron microscopy (SEM) images were taken with the InLens detector of a Zeiss LEO 1550 operating at 15 keV and 5.6 mm working distance. Thermal analysis was performed using a Netzsch STA 409 PC both under synthetic air and argon atmospheres at a heating rate of 10 °C/min.

Vibrational spectroscopy analyses were performed via dedicated IR and Raman equipment. Fourier Transform Infrared (FT-IR) spectroscopy was conducted through a Perkin-Elmer (Spectrum One) spectrometer to investigate a spectral region between 500 and 4000 cm⁻¹ using an attenuated total reflectance (ATR) mode. The IR spectra were collected through twenty cumulative acquisitions to improve the signal-to-noise (S/N) ratio and better highlight the spectral features of the material.

Raman spectroscopy was carried out by a Raman microscope (Renishaw – inVia) using an excitation wavelength of 532 nm generated by a laser diode (Renishaw) with a maximum output power of 500 mW. An initial calibration of the spectrometer was performed by means of a Si wafer to attain a characteristic reference peak around 520.6 cm⁻¹. The laser beam was focused on the surface of the sample by a 50× magnification objective and the measurements were conducted applying a constant laser power (0.1% of its maximum nominal value). Sixty cumulative scans were performed between 200 and 1600 cm⁻¹

with an acquisition time of 30 s to enhance the S/N ratio. Beam exposure minimization between subsequent scans was employed to avoid possible degradation of the specimen surface. Commercial powders of silver oxide (Ag_2O – Kebo) and iron (III) oxide hydroxide (FeOOH – Aldrich) were also employed as references for FT-IR and Raman analyses.

Electrode coating relied on a sodium salt of alginic acid (i.e. Na alginate, Aldrich – $M_w \approx 80000$ – 100000) as functional water-soluble polymer binder with the aim of using a renewable material to promote both simplicity and sustainability of this process. The slurry for electrode casting consisted of a mixture of AgFeO_2 nanoparticles as active material, Na-alginate as binder and carbon black (CB - C-Energy, C-65) as conductive additive. The electrode components had a 75:10:15 wt ratio for AgFeO_2 /Na-Alg/CB, respectively. This water-based slurry was cast on the rough side of a copper foil (Swedecal) using a coating machine (KR – K Control Coater). The coating was dried for 4 h at 80°C in a convection oven. After this consolidation step, circular electrodes with diameters of 20 and 13 mm were punched by means of dedicated perforators (Hohsen). Such coated discs had a thickness of about 8–10 μm for the coating, which was measured through a digital calliper (Mitutoyo), and a typical active mass loading of $\approx 0.67 \text{ mg cm}^{-2}$. Employing such thin electrode coatings ensures that the focus is on the actual electrochemical performances of AgFeO_2 as active material here, instead of possible kinetics effects arising from the electrode thickness. The resulting electrodes were subsequently dried in vacuum in a tubular vacuum oven (Büchi) at 120°C for 12 h before proceeding with cell preparation.

Polymer-laminated aluminium pouch cells were assembled in an Ar-filled glove box (M-Braun) having oxygen and moisture levels below 1 ppm. The pouches enclosed AgFeO_2 as working electrode, metallic lithium as concurrent reference- and counter-electrode and a LP40 electrolyte with 1 M LiPF_6 in ethylene carbonate (EC) and diethyl carbonate (DEC) with a EC:DEC 1:1 ratio. A thin porous membrane (Solupor) was soaked with this electrolyte and used as separator in these cells, which had Cu tabs as electrical contacts. An analogous battery configuration was used for the preparation of Na half-cells, where the only differences were the use of metallic sodium as reference- and counter-electrode and 1 M NaPF_6 as electrolyte salt dissolved in the same EC:DEC 1:1 solvent mixture.

Full Li-ion cells were built using a thin LFP-based coating as positive electrode. The latter was composed of C-coated LiFePO_4 (LFP P2 - SüdChemie), Na-alginate (Aldrich) and CB (C-Energy, C-65) with a 75:10:15 wt ratio, and cast on a carbon-coated aluminium foil (Leclanché - EB012 + Al 20 μm). These electrode coatings were dried in an analogous way as above. Coated discs with a diameter of 20 mm were employed for full cell preparation. Full cells were built using a protocol of direct pre-lithiation [4] for the AgFeO_2 electrode, which was first imbued with the electrolyte and then subjected to a firm contact with a metallic lithium strip. After 2 h, a deeply lithiated AgFeO_2 (i.e. reaching a converted/alloyed state) electrode was recovered and assembled in a pouch cell with Cu and Al contacts in combination with a LiFePO_4 positive counterpart, a separator and a few electrolyte drops.

Cyclic voltammetry (CV) was carried out via a VMP2 (Bio-Logic) equipment by applying a series of increasing sweep rates in the range of 0.1–1.6 mV s^{-1} to probe the electrochemical reactions in the potential window between 0.0 and 3.0 V vs. Li^+/Li or vs. Na^+/Na , respectively. Galvanostatic measurements were performed using a Digatron battery cycler (BTS600) by applying a constant current density of 0.05 mA cm^{-2} between 0.05 and 2.80 V vs. Li^+/Li or vs. Na^+/Na , respectively. Galvanostatic testing of the full cells was run on an MPG-2 (Bio-Logic) equipment utilizing a constant current density of 0.1 mA cm^{-2} with upper and lower cut-off voltages of 4.2 and 1.8 V, respectively. Rate capability of the full cells was tested employing a larger voltage window (4.2–1.6 V) and several current densities.

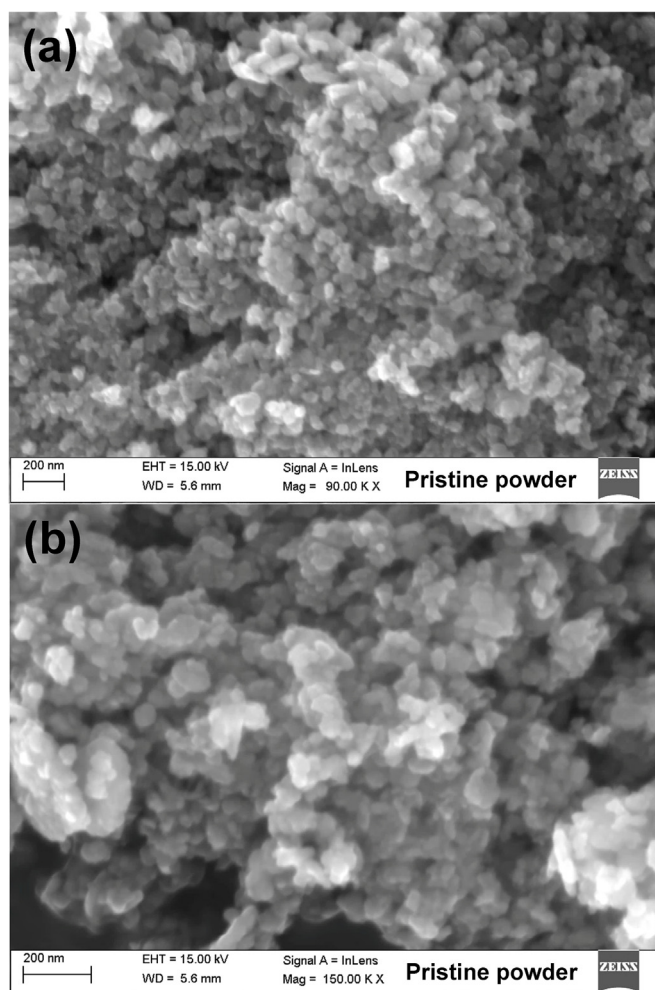


Fig. 1. SEM micrographs at different magnifications of pristine AgFeO_2 powders synthesized via precipitation.

3. Results and discussion

3.1. Structural and compositional analysis

Fig. 1 presents the SEM images of as-prepared AgFeO_2 powders. An evident nanostructured nature is noticed for the powders, which are composed of agglomerated particles, whose size roughly spans from 20 nm to 200 nm.

A certain degree of particle aggregation is also observed in Fig. 1, while different particle shapes are simultaneously present, e.g. spherical, platelet- and prismatic-like deposits to different extents. These features might arise from different crystal structures characterizing AgFeO_2 and possible presence of impurities.

Fig. 2a showcases the XRD pattern of the pristine AgFeO_2 powders.

The diffractogram exhibits different features with both sharp and broader peaks. The presence of both 3R (rhombohedral – JCPDF no. 01-075-2147) and 2H (hexagonal – JCPDF no. 01-070-1452) AgFeO_2 polytypes is clearly noticed from the peak assignment in Fig. 2a. This is a common feature of compounds with a Delafossite structure and for AgFeO_2 a mixture of 3R and 2H is always obtained via a precipitation route [15]. Both 3R and 2H structures consist of alternating layers of edge-sharing FeO_6 and close-packed Ag^+ , however, they possess a different plane-stacking sequence, as examined in detail in a recent synchrotron study [18] and schematically indicated in Fig. 2b–c. The

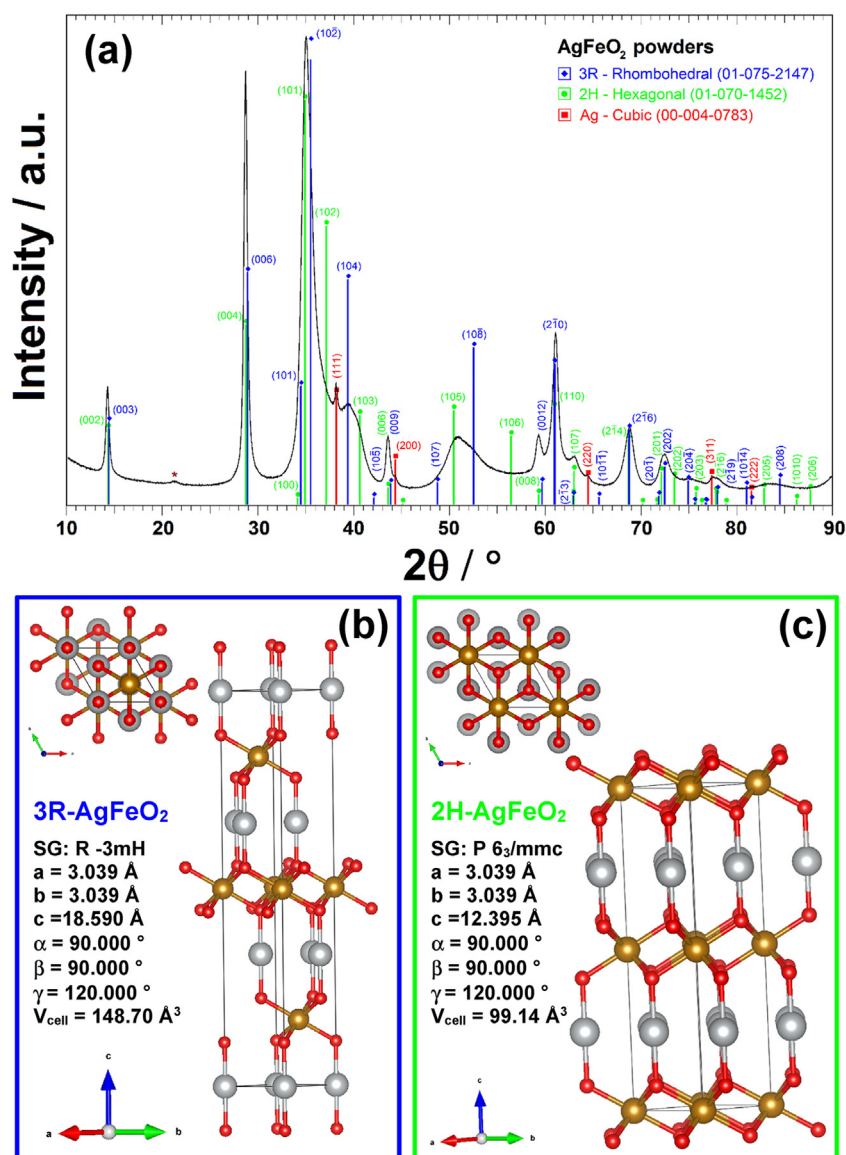


Fig. 2. (a) XRD pattern of pristine AgFeO₂ and assignment of the diffraction peaks. Overall structure and associated top-view along c-axis of rhombohedral (b) and hexagonal (c) AgFeO₂ polytypes. Ag, Fe and O atoms are represented by silver, brown and red spheres, respectively. Note that the asterisk around 20° in (a) is related with the most intense diffraction of α-FeOOH. (For interpretation of the references to colour in this figure legend, the reader is referred to the Web version of this article.)

pattern in Fig. 2a highlights a parallel existence of a minor impurity of crystalline Ag (JCPDF no. 00-004-0783), as indicated by the weak diffractions around 38.2°, 44.3°, 64.5°, 77.5° and 81.6°. Hence, a minor reduction of Ag⁺ to Ag⁰ seems to have occurred during the reaction in solution. This nanocrystalline Ag⁰ impurity will have a beneficial effect and improve the electrochemical reaction of AgFeO₂ from its early stages by decreasing the overall electrical resistivity of this material [78,79]. A weak feature around 21.1° (see asterisk in Fig. 2a) could not be associated with any diffraction of the previous crystalline phases. A closer inspection revealed that it originates from a minute impurity of α-FeOOH (JCPDF no. 29-713), which typically displays its most intense (110) diffraction in this angular range and is known to undergo a conversion reaction at low potentials vs. Li⁺/Li [80]. A satisfactory fit to the X-ray data could not be obtained with a multiphase Rietveld refinement, yet a profile fit suggests that the crystallite size is around 6 nm, which indicates that a large number of defects are present as stacking faults, in line with earlier results [18]. An indexing of the peaks that could be assigned to the 2H phase resulted in a unit cell with a = 3.0337 (2) Å, c = 12.4757 (4) Å and V = 99.43 (1) Å³. The large c

axis could suggest that there are no Ag vacancies or that it is constrained by the presence of the 3R phase, as c_{2H} = (2/3)c_{3R}.

Fig. 3 shows the results of the Raman analysis for the synthesized AgFeO₂ particles together with the spectra of commercial Ag₂O and FeOOH reference powders.

Two intense peaks are displayed around 350 cm⁻¹ and 639 cm⁻¹, which respectively correspond to characteristic E_g and A_{1g} modes [31,32] associated with a α-AgFeO₂, i.e. 3R-Delafossite structure (see Table 1). The E_g mode is associated with Fe-O-Fe bending, while the A_{1g} mode is related with Fe-O stretching vibration of the FeO₆ octahedra [31]. AgFeO₂ nanostructures typically exhibit a broad band in UV-vis measurements giving rise to strong absorptions in the range of 300–650 nm [31,33,34]. This feature makes them apt to both Resonant Raman Scattering (RRS) around 514 nm and to Surface Enhanced Raman Scattering (SERS) at higher wavelengths (e.g. 633 nm) as well [33]. In this case, using a 532 nm wavelength results in RRS and thus makes it possible to largely amplify not only the characteristic signals of the AgFeO₂ particles, but also those of other possible species near their surface. The synthesis of 100% pure AgFeO₂, in fact, is not necessarily

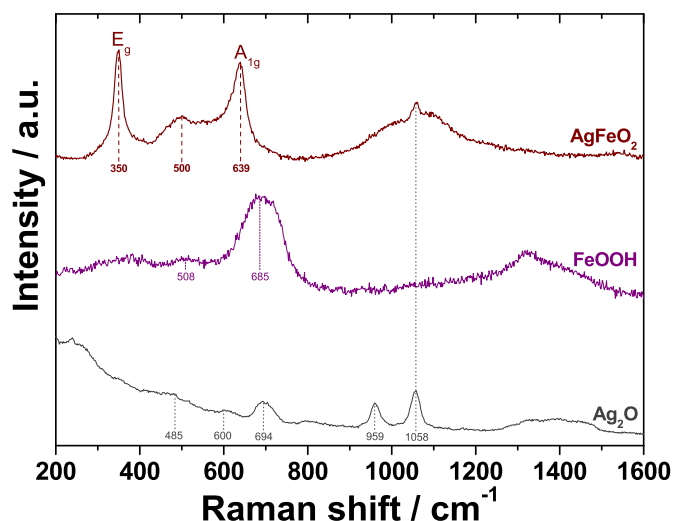


Fig. 3. Normalized Raman spectra of synthesized AgFeO_2 nanoparticles together with commercial FeOOH and Ag_2O powders taken here as references. Note the slight presence of Ag_2O impurity in the AgFeO_2 specimen.

straightforward, as minor impurities of Ag, Ag_2O and/or $\alpha\text{-FeOOH}$ are often found together with it [35], yet this is expected to favour the initial electrochemical reactions.

The spectrum of AgFeO_2 shows also some additional features around 501 cm^{-1} and 1058 cm^{-1} in Fig. 3. The peak at 1058 cm^{-1} can be attributed to a minor presence of Ag_2O and its passivated (i.e. carbonated [36]) surface, which matches with the XRD results, showing initial traces of Ag. This spectral contribution can be detected here thanks to the RRS. The other band around 500 cm^{-1} was previously observed in similar $\alpha\text{-AgFeO}_2$ powders [31], yet not assigned to any specific species. The XRD pattern in Fig. 2 revealed also the existence of 2H- AgFeO_2 and, so far, no dedicated Raman study has been focused on this hexagonal structure, apart from a previous investigation of AgFeO_2 thin films [37], where a tentative assignment of other peaks, possibly due to this 2H polytype, was proposed. A 2H structure possesses more Raman modes than its 3R counterpart and five Raman-active modes (i.e. $A_{1g} + E_{1g} + 3E_{2g}$) are expected for it (see Table 2), in agreement with earlier reports on layered oxides having the same space group $P6_3/mmc(194)$ [38–41].

The A_{1g} and E_{1g} modes for the 2H structure are associated with motions from O atoms only, similarly to the 3R polytype, whereas the vibrations from both Ag and O atoms can contribute to the E_{2g} modes. Hence, a simultaneous presence of 3R- and 2H- AgFeO_2 can also display some distinctive feature related with these E_{2g} modes, which could tentatively be assigned to the broad band around 500 cm^{-1} . Alternatively, this band could be attributed to Ag_2O , as this can match with a characteristic signature of this compound [36] in this spectral interval, considering the RRS. Crystalline $\alpha\text{-FeOOH}$ is also known to display some characteristic bands around 479, 550 and 685 cm^{-1} , yet its most intense peak is typically located at 385 cm^{-1} [42,43], thus it is not expected to play a major role here. Commercial FeOOH exhibited also a weak band in the wavenumber region around $470\text{--}550\text{ cm}^{-1}$, however, its normalized intensity was clearly lower than that of the

Ag_2O band around 485 cm^{-1} in Fig. 3. The asymmetric lineshape around 600 cm^{-1} for the peak in the AgFeO_2 spectrum could be related with Ag_2O traces, while the shoulder at the base of the A_{1g} mode, approximately around 700 cm^{-1} , could be equally attributed to an analogous A_{1g} vibration, due to the 2H polytype [37], and/or to Ag_2O and FeOOH impurities.

FT-IR measurements were performed to complement the previous results and obtain a clearer picture of the composition of the AgFeO_2 particles. Fig. 4 presents the FT-IR spectra of the AgFeO_2 particles and those of commercial FeOOH and Ag_2O powders, respectively.

The strongest IR absorption for the AgFeO_2 nanoparticles occurs around 598 cm^{-1} and this peak shows a slight shoulder at lower wavenumbers, too. This shoulder can arise from a minor contribution of Ag_2O , as this compound displays a maximum of IR absorption at 532 cm^{-1} in Fig. 4, in line with previous findings [36]. The peak at around 600 cm^{-1} is attributed to characteristic lattice vibrations of AgFeO_2 [35] together with another peak at 430 cm^{-1} , which is not detected here due to a minimum wavenumber threshold of 500 cm^{-1} . Theoretically, six IR-active modes are expected for the 3R- AgFeO_2 structure (see Table 1). These odd modes $A_{2u} + E_u$ are associated with acoustic phonons [31] and are distinct from the even ones, which are Raman-active, due to the existence of an inversion centre for this crystal structure. From Table 1, it is expected that the IR-active modes $A_{2u} + E_u$ due to the lattice vibrations of the Ag atoms should appear at low wavenumbers, since Ag is the heaviest element in this compound. Analogously, the $A_{2u} + E_u$ modes associated with the lattice vibrations of the Fe atoms should lie at low-mid wavenumbers and, ultimately, those of O atoms at higher ones. The second most intense absorptions in the IR spectrum of AgFeO_2 in Fig. 4 occur at 1347 cm^{-1} and 1468 cm^{-1} . These peaks are rather close in wavenumber position to those exhibited by commercial FeOOH (i.e. 1349 and 1492 cm^{-1}). However, it would be questionable that a minor FeOOH impurity in AgFeO_2 can show a more intense and defined IR signal in this layered compound rather than in its purest form. Besides, characteristic IR spectra of crystalline $\alpha\text{-FeOOH}$ substantially differ from the one of commercial powders, presenting only prominent peaks around 890 and 780 cm^{-1} , while appearing featureless between 1200 and 1600 cm^{-1} [35,44], unless containing small amounts of carbonate anions [45]. The features at 1347 cm^{-1} and 1468 cm^{-1} appear also distinct from the peaks displayed by Ag_2O around 1323 cm^{-1} and 1398 cm^{-1} , which are possibly associated with silver carbonates on its surface together with other weaker peaks at 721 , 802 and 1071 cm^{-1} [36]. Hence, it would be reasonable to assign the peaks at 1347 cm^{-1} and 1468 cm^{-1} to characteristic lattice vibrations of AgFeO_2 , because the attribution of these IR absorptions to $\alpha\text{-FeOOH}$ or $\text{Ag}_2\text{O}/\text{Ag}_2\text{CO}_3$ impurities does not match closely with the strength and positions of their characteristic signals, respectively. Moreover, the presence of 2H- AgFeO_2 cannot be neglected, as the latter is expected to contribute with a series of IR modes (see Table 2), too. Similar peaks in the spectral range of $1280\text{--}1580\text{ cm}^{-1}$ were also detected previously in the IR spectrum of pure AgFeO_2 [34], although no assignments were made. The remaining faint peaks/bands in the spectrum of AgFeO_2 in Fig. 4 are due to slight impurities of $\text{Ag}_2\text{O}/\text{Ag}_2\text{CO}_3$ around 1069 cm^{-1} [36] and $\alpha\text{-FeOOH}$ in proximity of 888 cm^{-1} and 780 cm^{-1} [35], whereas the other features could be associated with vibrations of the 2H structure. A presence of water in the AgFeO_2 powders was also found. Distinctive bands around

Table 1

Synoptic table of atomic site positions for each constituent element, associated site symmetries and phonon modes of 3R- AgFeO_2 .

Atoms	Atomic coordinates	Wyckoff symbol	Site symmetry	Associated representations	Raman modes	Infrared modes
Ag	(0,0,0)	3a	D_{3d}	$A_{2u} + E_u$	–	$A_{2u} + E_u$
Fe	(0,0,1/2)	3b	D_{3d}	$A_{2u} + E_u$	–	$A_{2u} + E_u$
O	(0,0,z)	6c	C_{3v}	$A_{1g} + A_{2u} + E_g + E_u$	$A_{1g} + E_g$	$A_{2u} + E_u$

Space group: $R\bar{3}m H(166)$; $z = 0.112(5)$.

Table 2

Synoptic table of atomic site positions for each constituent element, associated site symmetries and phonon modes of 2H-AgFeO₂. Note the existence of two distinct sites for Ag.

Atoms	Atomic coordinates	Wyckoff symbol	Site symmetry	Associated representations	Raman modes	Infrared modes
Ag1	(1/3,2/3,1/4)	2d	D _{3h}	A _{2u} + B _{1g} + E _{1u} + E _{2g}	E _{2g}	A _{2u} + E _{1u}
Ag2	(0,0,1/4)	2b	D _{3h}	A _{2u} + B _{1g} + E _{1u} + E _{2g}	E _{2g}	A _{2u} + E _{1u}
Fe	(0,0,0)	2a	D _{3d}	A _{2u} + B _{2u} + E _{1u} + E _{2u}	-	A _{2u} + B _{2u} + E _{1u} + E _{2u}
O	(1/3,2/3,z)	4f	C _{3v}	A _{1g} + A _{2u} + B _{1g} + B _{2u} + E _{1g} + E _{1u} + E _{2g} + E _{2u}	A _{1g} + E _{1g} + E _{2g}	A _{2u} + B _{2u} + E _{1u} + E _{2u}

Space group: P6₃/mmc(194); z = 0.083(3).

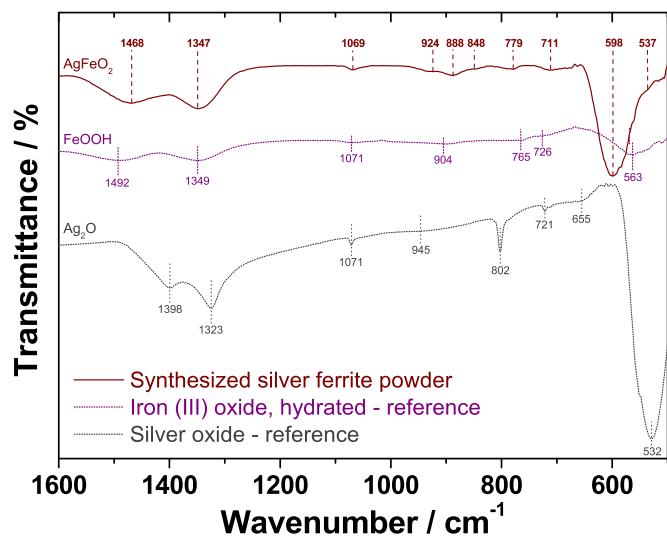


Fig. 4. FT-IR spectra of synthesized AgFeO₂ nanoparticles together with commercial FeOOH and Ag₂O powders taken here as references.

3330 cm⁻¹ and 1647 cm⁻¹ were detected at higher wavenumbers and thermal analyses (TGA, DTA) confirmed this finding (see Fig. S1 and Fig. S2 in Supporting Information – SI).

3.2. Electrochemical analysis

The electrochemical properties of the AgFeO₂ nanoparticles were investigated through cyclic voltammetry (CV) in Li half-cells. Fig. 5 presents various voltammograms obtained with a composite AgFeO₂ electrode undergoing a series of cycles. Fig. 5a shows the initial cycles at a sweep rate of 0.1 mV s⁻¹ between 0.0 and 3.0 vs. Li⁺/Li.

In the first cathodic half-cycle, two main reductive features are noticed upon progressive incorporation of Li⁺ from the open circuit voltage (OCV) to 0.0 V. The prominent peak around 1.7 V is due to an irreversible structural change of AgFeO₂ caused by the reduction of Ag⁺ to Ag⁰, as reported in earlier studies [14,15,17]. This process causes the formation of small metallic Ag nanoparticles [14] through a progressive removal of the silver ions from the Delafossite structure, thereby giving rise to an irreversible amorphization of its original crystal lattice. The asymmetric shape of this cathodic peak around 1.6 V suggests the presence of a slight shoulder, which was earlier ascribed to a partial Fe³⁺ → Fe²⁺ reduction [14]. The main cathodic peak around 0.75 V in Fig. 5a is caused by a further reduction of most of Fe²⁺ → Fe⁰ (i.e. oxide conversion and generation of Li₂O – see Fig. S7 in SI) accompanied by irreversible formation of a solid electrolyte interphase (SEI) [18,46]. An initial Li-alloying of earlier-formed Ag nanoparticles could also take place in this voltage range. In fact, a shift in the electrochemical potential of metallic nanoparticles typically occurs as their size shrinks down to a few nanometers [47] and small Ag nanoparticles are known to undergo significant oxidative shifts in electrochemical reactions in water solutions [48,49]. Li-Ag alloy formation for pure Ag particles or films typically starts at potentials below 0.25 V in

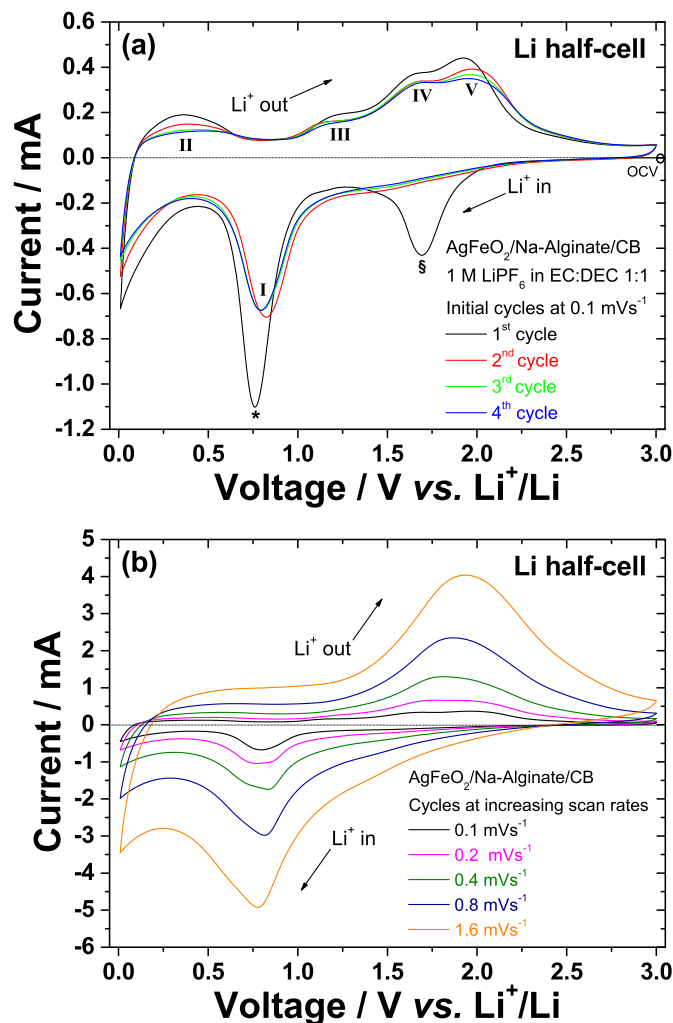


Fig. 5. (a) Cyclic voltammograms for a composite AgFeO₂ electrode cycled in a Li half-cell with a sweep rate of 0.1 mV s⁻¹ between 0.0 and 3.0 V vs. Li⁺/Li. (b) Series of CV cycles obtained by applying increasing sweep rates from 0.1 to 1.6 mV s⁻¹ in the same range of potentials. Note that the positions of the red-ox peaks in (b) are not sensibly shifted upon application of higher scan rates. (For interpretation of the references to colour in this figure legend, the reader is referred to the Web version of this article.)

galvanostatic experiments and proceeds extensively down to 0.0 V vs. Li⁺/Li [28,29,50–52]. Here, Li-Ag alloying appears to begin earlier and this is possibly highlighted by an asymmetric shape of the main cathodic peak, which displays a slight shoulder around 0.6 V. This process continues at lower potentials in Fig. 5a and contributes to the rise in cathodic current from ≈0.5 V down to 0.0 V, together with the pseudocapacitance [53] generated by Fe/Li₂O phase boundaries [54–56]. The first anodic half cycle in Fig. 5a shows a series of bumps and peaks related to reverse oxidative processes undergone by the Li-Ag alloy and Fe/Li₂O nanocomposite, respectively. The first anodic feature

around 0.4 V (peak 'II') can be ascribed to initial de-alloying and Li^+ release [29,50–52] which occur in a two-step fashion giving rise to a broad oxidation band around 1.25 V (peak 'III'). The latter overlaps the de-conversion of $\text{Fe}/\text{Li}_2\text{O}$, which takes place in two stages (peak 'IV' and 'V') and typically leads to the formation of iron oxide nanoparticles [46,57]. At the end of the anodic scan at 3.0 V, a different material is obtained, as the cycled AgFeO_2 has practically lost its Delafossite structure and consists of a mixture of small metallic silver and lithium iron oxide nanoparticles, instead (see *post mortem* XRD analysis in Fig. S5, HR-TEM in Fig. S6 and HAADF-STEM in Figs. S8 and S9 in SI). After the first cycle, a part of the charge is irreversibly lost, not only because of the SEI formation, but also due to a minimal oxidation of the silver. The latter cannot be re-oxidized [14], as it is inferred from the absence of a cathodic peak around 1.7 V in the following CV cycles. This has recently been confirmed by accurate EXAFS measurements/modelling [18] and is detrimental for charge recovery. Nevertheless, the in situ formation of an extensive electronically conductive network of Ag nanoparticles during the initial lithiation stages has been shown to yield a huge decrease (i.e. ≈ 6000 -fold) of the overall resistivity of this type of electrodes [16,26,58]. The position of the main cathodic peak ('I') is slightly shifted to ≈ 0.8 V in the following cycles, unlike the majority of binary transition metal oxides upon conversion [19,59], and its shape becomes more symmetrical, too. A rather similar behaviour for the reductive peak in the first half-cycle was observed previously for small amorphous Fe_2O_3 nanoparticles [27,60–62]. The respective anodic features remain almost unchanged in Fig. 5a, apart from a minor fading and slight shift of the last peak ('V') at higher voltage with progressive cycling. The impact of these in situ-formed Ag nanoparticles on the electrode behaviour can be better appreciated in Fig. 5b, which shows a series of subsequent cycles run at increasing scan rates.

Both cathodic and anodic peaks intensify their absolute currents and get progressively broader as well. However, their respective peak potentials do not shift substantially with the sweep rates. The application of increasing sweep rates typically results in a shift of the anodic peaks towards higher voltages (and of their cathodic counterparts towards lower ones), if their processes are limited by charge transfer and/or IR drop [63]. This effect is minor here compared to other binary iron oxide electrodes undergoing this analysis with analogous scan rates [46,64]. This suggests that the overall resistance of the AgFeO_2 electrode remains rather low during cycling after the Ag nanoparticle generation, because an increase in the red-ox peak current does not cause a neat simultaneous change for its associated potential - as required by Ohm's law - if resistance were a rate-limiting factor here. Considering the nearly linear behaviour of the peak currents with the scan rates (see Fig. S3 in SI), it can be inferred that this electrode mostly operates under thin-film electrochemical conditions [63]. The processes are mainly surface-controlled in this regime yielding a capacitive-like charge storage. Hence, a pseudocapacitive behaviour [53], characteristic of conversion reactions generating here $\text{Fe}/\text{Li}_2\text{O}$ boundaries [54,55,65,66], appears to be supported by these Ag nanoparticles, which are finely inter-dispersed in clusters with Fe^0 (see Fig. S7 in SI). They remain in a metallic state during the lithiation and formation of $\text{Fe}/\text{Li}_2\text{O}$, undergoing Li-Ag alloying at lower voltages, although the detection of such Li-Ag compositions was challenging (see Figs. S5, S7 and S8 in SI). Vice versa, their early de-alloying upon Li^+ removal reforms Ag^0 , thus assisting subsequent de-conversion of $\text{Fe}/\text{Li}_2\text{O}$. However, these alloying/de-alloying Ag nanoparticles on the electrode surface could play also a destabilizing role for the SEI, as this passivating layer needs to be electronically insulating, while offering a high ionic conductivity for Li^+ entering/leaving the active material. Fig. 5b and Fig. S3 in SI show that the cathodic peak currents are always higher than their anodic counterparts, thereby suggesting that some parasitic processes could be involved as well.

Carrying out the same CV analysis on a composite AgFeO_2 electrode in a Na half-cell shows clear differences in the electrochemical response, as observed in Fig. 6.

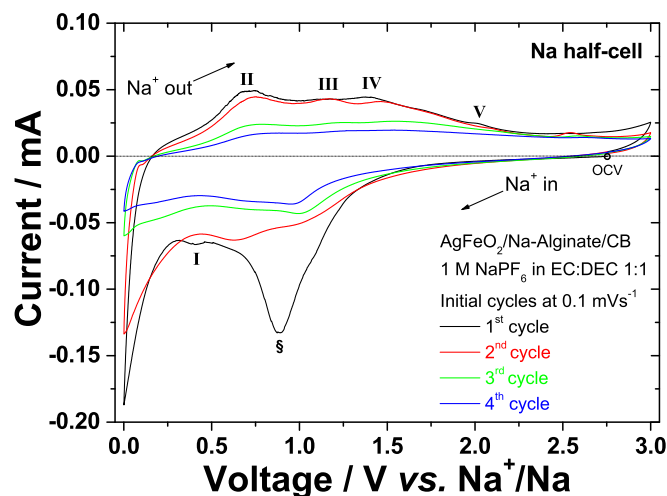


Fig. 6. Cyclic voltammograms for a composite AgFeO_2 electrode cycled in a Na half-cell with a sweep rate of 0.1 mV s^{-1} between 0.0 and 3.00 V vs. Na^+/Na . Note the similarities and differences with the CV cycles shown in Fig. 5a and a clear irreversibility of the red-ox processes leading to a quick loss of capacity. (For interpretation of the references to colour in this figure legend, the reader is referred to the Web version of this article.)

The extent of the reactions appears limited and an initial, irreversible $\text{Ag}^+ \rightarrow \text{Ag}^0$ reduction in the Delafossite structure takes place at much lower voltages vs. Na^+/Na (i.e. ≈ 0.9 V), suggesting a larger overpotential upon sodiation compared to its analogous lithiation. Its cathodic peak exhibits a broad and asymmetric shape because also other concomitant reactions (e.g. $\text{Fe}^{3+} \rightarrow \text{Fe}^{2+}$ reduction [46] and SEI formation [67]) take place in this voltage range. Only a small bump is noticed in Fig. 6 around ≈ 0.4 V in the first cathodic scan and this could be ascribed to the onset of a conversion mechanism with initial generation of $\text{Fe}/\text{Na}_2\text{O}$ [46,64]. Most likely, this early conversion stage does not reach its completion [46,64,68], as it can be inferred from the limited current yielded by this cathodic feature. Conversely, Na-Ag alloying of the Ag nanoparticles manifests more clearly at lower voltages and accounts for the highest cathodic current at 0.0 V vs. Na^+/Na . The de-alloying upon Na^+ release in the first anodic scan is also evident around ≈ 0.6 V and continues up to ≈ 1.2 V giving rise to a slight bump. A feeble de-conversion of $\text{Fe}/\text{Na}_2\text{O}$, due to iron oxidation, occurs at higher voltages in a way similar to that seen in Fig. 5a.

The main differences in the electrochemical behaviour of AgFeO_2 in presence of Li^+ or Na^+ are its reversibility, as well as the extent of conversion and Li-/Na-alloying. The following cycles in Fig. 6 exhibited a rapid fade of the red-ox processes, thus causing irreversible capacity losses. Hence, it can be argued that exploiting this compound for Na storage is more challenging than employing it in LIBs (see also Fig. S4 in SI). The in situ formation of the Ag nanoparticles upon sodiation did not promote a full conversion into $\text{Fe}/\text{Na}_2\text{O}$, as the initial capacity was rather limited (see Fig. S4 in SI). Na-Ag alloying, appeared to be more favourable, instead. These differences can be rationalized considering a series of key factors, namely, *i.* distinct radii of Li^+ and Na^+ , *ii.* different standard reduction potentials for Li^+/Li and Na^+/Na , *iii.* similarities in Ag-Li vs. Ag-Na phase diagrams [69–72], *iv.* distinctive reactivity of lithium and sodium metals towards their respective electrolytes [73] and *v.* ability of the latter to form/stabilize a SEI layer [67,74] on this ternary oxide.

The early presence of Ag in AgFeO_2 is attractive not only to boost the electrical conductivity of this compound upon reaction, but also to enhance its ultimate capacity. Indeed, the Ag-Li phase diagram [69,70] suggests a series of possibilities for Li storage around room temperature, since intermetallic compounds with high lithium contents (e.g. Li_2Ag , Li_3Ag and even Li_{12}Ag) can be formed, although electrochemical Li-Ag alloying typically does not reach such high (e.g. > 3) Li compositions

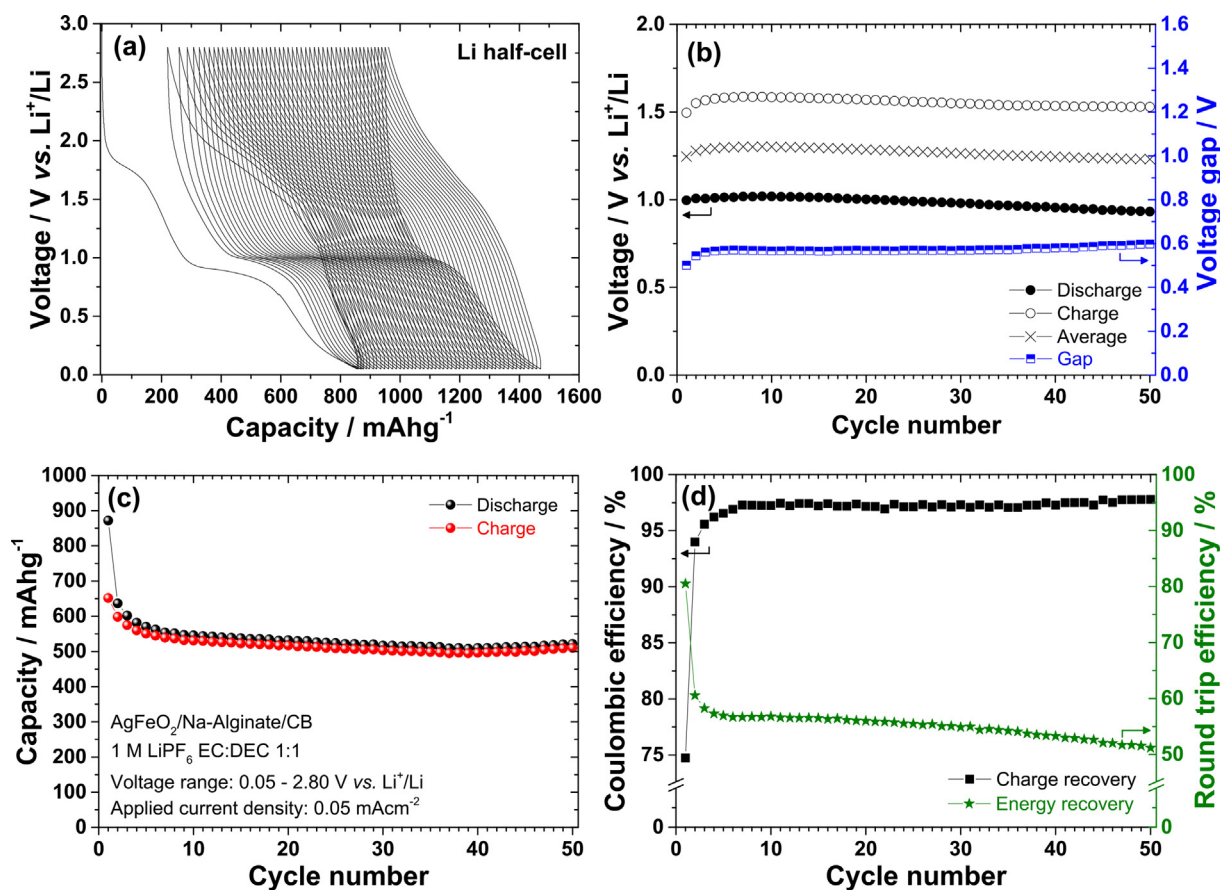


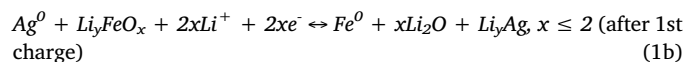
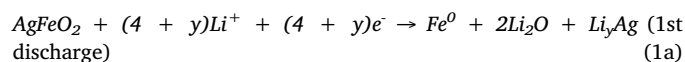
Fig. 7. (a) Galvanostatic discharge/charge profiles for a composite AgFeO₂ electrode cycled in a Li half-cell between 0.05 and 2.80 V vs. Li⁺/Li with a current density of 0.05 mAcm⁻². (b) Evolution of the average values of discharge and charge potentials per cycle. (c) Cycle performance showing the evolution of discharge/charge capacities. (d) Coulombic and round-trip efficiencies for each discharge/charge cycle.

[24,28,29,50,51]. This scenario is clearly different for the Ag-Na phase diagram [71,72], where the main intermetallic product is represented by AgNa₂ Laves phase.

Galvanostatic tests of these AgFeO₂ electrodes were carried out in Li- and Na half-cells to assess more in detail the extent of the respective reactions and clarify the mechanisms behind their different electrochemical behaviour. Both tests employed a low current density of 0.05 mAcm⁻² to allow enough time for the reactions to take place. Fig. 7 presents the galvanostatic cycling results of AgFeO₂ in a Li half-cell between 0.05 and 2.80 V vs. Li⁺/Li, while those related to the Na half-cell are shown in Fig. S4 in SI.

The characteristics exhibited by the discharge/charge profiles in Fig. 7a are in accord with the previous CV findings. The first plateau at ≈1.75 V vs. Li⁺/Li upon discharge is irreversible and confirms that permanent changes take place due to the Ag⁺ → Ag⁰ reduction. This process yields a capacity of 155 mAhg⁻¹ at a depth of discharge of 1.6 V, in line with previous reports [14]. The theoretical capacity arising from the incorporation of x = 1 mol of Li into AgFeO₂ - to form a hypothetical Li_xAgFeO₂ compound - corresponds to 137 mAhg⁻¹. Hence, a minor contribution to the observed capacity can be ascribed to a partial Fe³⁺ → Fe²⁺ reduction, as mentioned above. A nearly linear profile of the first discharge curve is noticed up to ≈1.0 V, which provides a capacity of 275 mAhg⁻¹. The latter corresponds to x ≈ 2 mol of Li uptake in the original material and can be linked to a progressive reduction of Fe³⁺ to Fe²⁺. The prominent plateau below 1.0 V, extending down to ≈0.70 V, confirms the presence of irreversible capacity losses in the first cycle, which ensue from the SEI formation accompanying the Fe²⁺ → Fe⁰ reduction and Li₂O formation (see Fig. S7 in SI). In fact, this plateau is not equally pronounced in the subsequent

cycles and shifts to slightly higher voltages, too. These results corroborate the previous findings showing that with increasing lithiation a progressive destruction of the AgFeO₂ lattice occurs in two key steps: *i.* irreversible Ag⁺ reduction-displacement from the pristine structure and formation of Ag⁰ nanoparticles (x = 1) followed by Fe³⁺ → Fe²⁺ reduction (1 ≤ x < 2), *ii.* conversion of the remaining oxide generating Fe/Li₂O (x ≥ 2) and subsequent Li-Ag alloying. The alloying proceeds at low potentials and overlaps the characteristic pseudocapacitive charge storage of Fe/Li₂O in Fig. 7a, as seen from the ending part of the discharge curve below 0.70 V and its curvature change around 0.25 V. The capacity obtained at the end of the first discharge is 872 mAhg⁻¹ (≈6.4 Li moles per AgFeO₂ formula unit) and this value was delivered in about 11 h and 30 min, thus corresponding to ≈ C/11.5 rate). The Li-Ag alloying reaction, at least in principle, might be not fully complete at 0.05 V, as for pure Ag a substantial reaction is often noticed below 100 mV vs. Li⁺/Li [29,50–52]. However, looking back at the ending part of the CV curve in Fig. 5a (i.e. very close to 0.0 V vs. Li⁺/Li in the first cathodic half-cycle) and considering that only small Ag nanoparticles are formed, the additional capacity due to remaining alloying in a full discharge to 0.0 V should be negligible. Hence, taking into account the charge irreversibly consumed by the SEI, an overall reaction involving the full conversion of this oxide into Fe⁰ and Li₂O accompanied by the generation of Li_yAg can reasonably be expected:



This corresponds to a theoretical capacity of 685 mAhg⁻¹ in eq. (1a)

for $y = 1$, deriving from a cumulative storage of 5 mol of Li per AgFeO_2 formula unit (see also details in section S1 in SI). The irreversible capacity, mostly due to the SEI formation, is rather low here (187 mAhg^{-1}), especially if compared with previous reports involving similar nano-sized materials [27]. A good reversibility of the initial reaction (eq. (1b)) is suggested by the capacity recovered at the end of the first charge ($\approx 650 \text{ mAhg}^{-1}$). The latter would correspond to $\approx 94.9\%$ of its initial theoretical value (i.e. 685 mAhg^{-1}) and yields in practice a moderate Coulombic efficiency of $\approx 74.5\%$ (Fig. 7d). The formation of a reversible Li_yAg alloy with y closer to 1 instead of 2 is also likely here, as a Li_2Ag intermetallic would yield an overall theoretical capacity of 822 mAhg^{-1} for AgFeO_2 , meaning that only 50 mAhg^{-1} would be irreversibly consumed by the SEI. Such an extremely low loss is not plausible here, especially considering the nanostructured nature of the reacting materials and their large interface contact with the electrolyte, as well as the presence of the carbon black. Hence, the formation of Li_2Ag , if any, is marginal based on the capacity values of the first charge in Fig. 7a and the features of the first cathodic half-cycle in Fig. 5a.

The profile of the first charge in Fig. 7a highlights an inflection at $\approx 0.60 \text{ V}$ and the presence of two slight features around $\approx 0.25 \text{ V}$ and $\approx 1.10 \text{ V}$, respectively. This matches well with the previous findings in Fig. 5a and corroborates the above picture that de-alloying readily happens at low voltages to re-form Ag nanoparticles (see also Figs. S5, S8 and S9 in SI), whereas de-conversion and generation of lithium iron oxide (i.e. LiFeO_2 – see Fig. S5 in SI) nanoparticles require higher voltages (see sloping part of the charge curve between $\approx 1.30 \text{ V}$ and $\approx 2.00 \text{ V}$ in Fig. 7a). A continuous shift of the discharge/charge profiles along the horizontal axis in Fig. 7a reveals the presence of parasitic processes affecting the capacity in each cycle. This is clearly seen in Fig. 7d, where the Coulombic efficiency is far from 100% and reaches only $\approx 97.7\%$ after 50 cycles. The capacity after 50 cycles is $\approx 520 \text{ mAhg}^{-1}$ in Fig. 7c, supporting the idea that the overall reaction in eq. (1b) is moderately reversible, although the electrochemical processes involved in it affect to some extent the electrolyte. In fact, the discharge capacities are always higher than their charge counterparts, suggesting a continuous electrolyte consumption. The role of the Ag nanoparticles appears beneficial, as it helps decreasing the resistivity of the entire electrode upon reaction, while it does not seem to promote a simultaneous SEI stabilization. The impact of these Ag nanoparticles on the oxide conversion/de-conversion process is negligible in terms of round trip efficiency per cycle (see Fig. 7d), since the latter remains below 60% after the first cycle. This implies that even a significant increase of the electronic conductivity does not actually improve the energy efficiency of this type of reaction, which is most likely limited by intrinsic thermodynamic constraints [20] due to the generation of small metal nanoparticles and their extensive phase boundaries. A clear hysteresis of the charge/discharge curves is noticed in Fig. 7a, giving rise to an average voltage gap of $\approx 0.6 \text{ V}$ (Fig. 7b), which is in line or slightly lower than that of several other transition metal oxides. The average operational voltage of AgFeO_2 displays values close to 1.25 V vs. Li^+/Li in each cycle in Fig. 7b and this makes it of limited use as negative electrode, if cycled under such testing conditions demanding a large voltage window for its conversion and de-conversion. Conversely, the synergy of its pseudo-capacitive charge storage and Li-alloying at low potentials vs. Li^+/Li could make it suitable as alternative negative electrode in full Li cells, provided that energy losses are minimized. With these ideas in mind, deeply lithiated AgFeO_2 via direct contact pre-lithiation [4] was tested as negative electrode in full cells against LiFePO_4 (LFP) and cycled between 1.8 and 4.2 V (see Fig. 8).

Fig. 8a shows the voltage profiles of charge/discharge of a full cell for the first 50 cycles. The initial sloping plateau on charge, due to Li^+ extraction from LFP, is located around 3.5 V, thus demonstrating that the deeply lithiated AgFeO_2 operates at potentials very close to that of metallic lithium. However, the charge/discharge plateaus became progressively more sloping with cycling. This phenomenon was

reported earlier and related with size effects arising from the presence of a distribution of metallic nanoparticles [4]. Here, two key contributions are simultaneously at play for this deeply lithiated AgFeO_2 : *i.* Fe nanoparticles, which do not alloy with Li, and *ii.* alloying/de-alloying Ag clusters, which can accept/release Li through the formation/dissolution of Li_yAg . Fig. 8a highlights a small progressive shift of the charge/discharge profiles along the horizontal axis, thereby implying a possible initial presence of some parasitic process also in this case. Nevertheless, the performances of this full iron-based battery are interesting. The presence of the Ag nanoparticles in the negative electrode is advantageous and this is clearly reflected in the low hysteresis upon cell charge/discharge at a rate of $\approx 1.4\text{C}$ (i.e. full charge in $\approx 42 \text{ min}$). The average charge/discharge voltages in Fig. 8b varied only slightly during the first 150 cycles, while such values were stable afterwards and an average operational voltage of 3.0 V was achieved. To the best of our knowledge, this is so far one of the highest operational voltages for this type of LFP-based cells [4] not including a graphite negative electrode. More remarkable is the narrow voltage gap between charge and discharge in each cycle, whose values remained as low as $\approx 0.1 \text{ V}$ after 1000 cycles in Fig. 8b. This key feature is unmatched by similar cells with LFP relying either on ternary iron-based oxides undergoing both conversion and alloying [75,76] or binary iron oxides such as $\text{Fe}_3\text{O}_4/\gamma\text{-Fe}_2\text{O}_3$ [4] and $\alpha\text{-Fe}_2\text{O}_3$ [77]. The charge and discharge capacities (referred to the active LFP mass) in Fig. 8c were close to 140 mAhg^{-1} during the first 15 cycles, in which a slight capacity increase was noticed. The capacity retention of the full cell is clearly good and, although a continuous fading after the first 15 cycles is observed in Fig. 8c, its ultimate discharge capacity was almost 110 mAhg^{-1} , thus very close to 80% of its maximum initial value. This is satisfactory, especially considering that no additive or particular electrolyte formulation was employed here. The reasons behind the capacity fading are not entirely clear and another in-depth study would be necessary to pinpoint such phenomenon. Nevertheless, possible parasitic reactions could constitute a source for this fading, as suggested by the values of both Coulombic and round trip efficiencies in Fig. 8d. The Coulombic efficiency was not 100% and had an average value of 99.6% over 1000 cycles. The round trip efficiency increased during the first 30 cycles to reach a maximum value of $\approx 92\%$, while it declined with subsequent cycling to $\approx 87\%$ at the end of the test. The average round trip efficiency over 1000 cycles was 88.8%, which proves an excellent result, especially considering the intrinsic limitations for the energy efficiency of AgFeO_2 in Li half-cells (see Fig. 7).

The rate capability of these full cells was also probed by running a series of charge/discharge cycles between 4.2 and 1.6 V with different current densities (see Fig. S10 in SI). The results indicate that this type of cell can be cycled to C-rates as high as $\approx 25\text{C}$ with a good capacity retention for its LFP cathode (i.e. $\approx 85 \text{ mAhg}^{-1}$) and recovering most of its capacity (i.e. $\approx 160 \text{ mAhg}^{-1}$) when subsequently cycled to lower rates of $\approx \text{C}/10$.

All in all, the Ag nanoparticles originating from AgFeO_2 have a clear impact on the cycling of this compound and justify the inclusion of small amounts of Ag particles in iron oxides to improve their electrical properties [27], as well as a possible use of $\text{Ag}_x\text{Fe}_y\text{O}_z$ composites made of crystalline AgFeO_2 and amorphous $\gamma\text{-Fe}_2\text{O}_3$ [15,16,26] with lower silver contents ($x < 1$). From the above results, it is clear that AgFeO_2 can conveniently be utilized in Li-ion cells with LFP in its fully lithiated form, thus avoiding cyclical conversion/de-conversion, while retaining a beneficial combination of the properties arising from in situ formed nanoparticles of different metals promoting complementary functionalities. This gives an opportunity to exploit better the pseudocapacitance arising from the Fe/ Li_2O boundaries and the Li-alloying/de-alloying of the Ag nanoparticles, while enhancing the operational voltage of the full cell, its energy efficiency and ability to undergo fast charge/discharge.

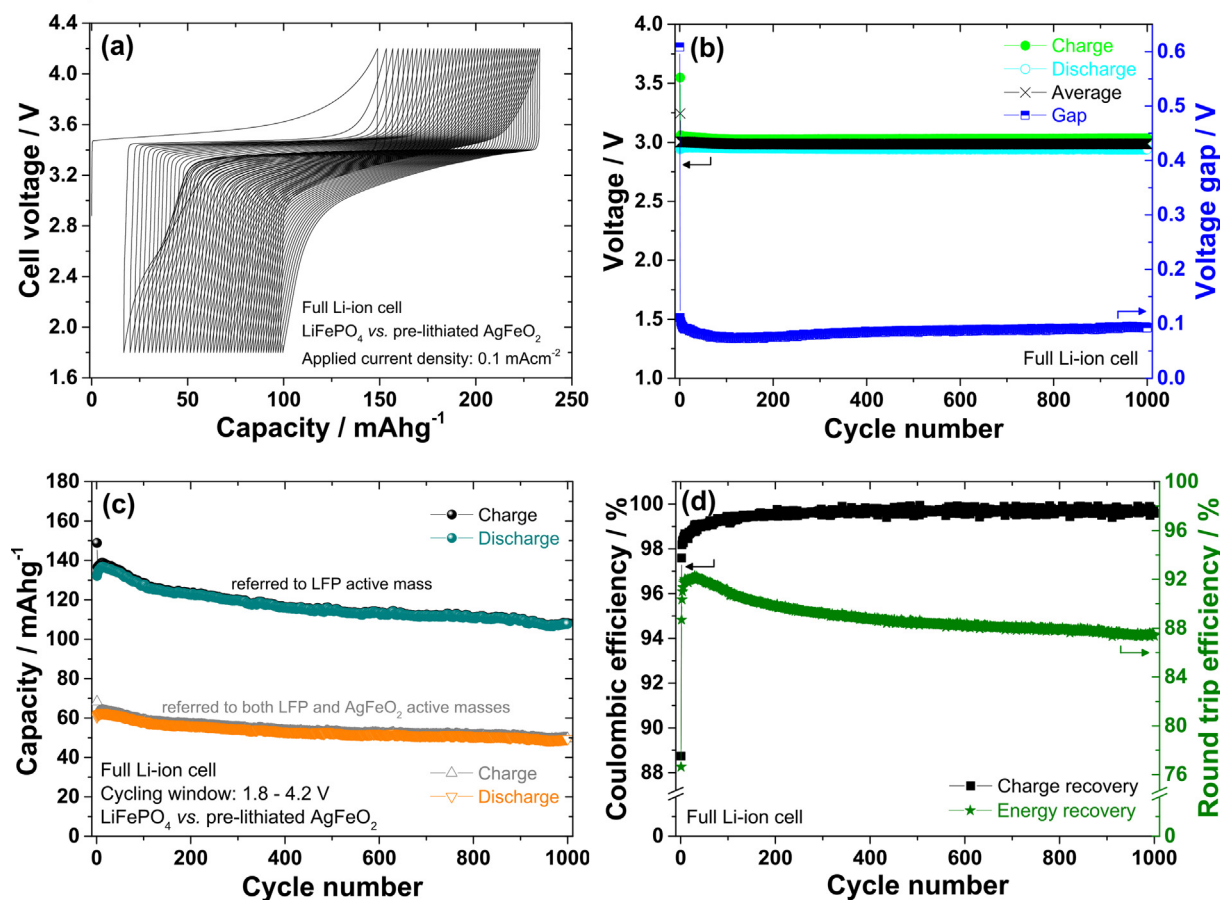


Fig. 8. (a) Galvanostatic charge/discharge profiles of a full cell having LiFePO₄ as positive electrode and deeply lithiated AgFeO₂ as negative counterpart cycled with a standard 1 M LiPF₆ electrolyte between 1.8 and 4.2 V at a current density of 0.1 mAcm⁻². (b) Evolution of the average values of charge and discharge potentials of the full cell in each cycle. (c) Cycle performance showing the evolution of charge/discharge capacities of the full cell. (d) Coulombic and round-trip efficiencies of the full cell. Note the low voltage gap between the charge and discharge values in (b) and the good round-trip efficiency in (d).

4. Conclusions

The electrochemical behaviour of AgFeO₂ as alternative negative electrode in Li- and Na-ion batteries was investigated in detail for the first time via composite coatings employing a Na-alginate binder. Nanostructured AgFeO₂ was synthesized at room temperature via a precipitation method enabling the formation of crystalline nanoparticles of this Delafossite-type compound. This approach provided a mixture of rhombohedral (3R) and hexagonal (2H) structures for AgFeO₂ together with some minor traces of crystalline Ag and α -FeOOH, which are favourable for its reactions.

The results for initial reaction with Li⁺ ions confirmed that Ag⁺ cations in AgFeO₂ are progressively removed in an irreversible reduction-displacement from its layered structure to form Ag⁰ nanoparticles around 1.7 V vs. Li⁺/Li. A similar irreversible mechanism was also found upon reaction with Na⁺ ions. However, the Ag reduction-displacement took place around 0.9 V vs. Na⁺/Na, thus showing a significant overpotential upon sodiation. Progressive discharge to lower potentials vs. Li⁺/Li and vs. Na⁺/Na resulted in distinctive features for respective half-cells. The incorporation of $x > 2$ mol of Li caused the conversion of its original FeO₆ units into Fe⁰ nanoparticles and Li₂O with a concomitant SEI formation around 0.8 V. Further reaction at lower voltages gave rise to Li-Ag alloying of the Ag⁰ nanoparticles.

Subsequent reaction of AgFeO₂ with Na⁺ below 0.9 V resulted instead in very poor oxide conversion, while Na-Ag alloying was observed close to 0 V vs. Na⁺/Na. A limited capacity at the end of the first discharge demonstrated a clear hindrance for complete reactions upon sodiation, differently from lithiation. The cycle performances of Li- and

Na-half cells also indicated a superior cycleability of AgFeO₂ with Li⁺ ions, displaying a good capacity retention after 50 cycles, despite the existence of possible parasitic processes.

The in situ generation of Ag⁰ nanoparticles upon lithiation proved beneficial, as this boosted the overall electronic conductivity of the electrode and contributed to its storage capacity via Li-Ag alloying. The latter operated in synergy with a pseudo-capacitive charge storage below 0.5 V vs. Li⁺/Li, thereby offering an effective uptake/release of Li⁺ ions (and electrons) at potentials close to the Li⁺/Li couple. This key feature was exploited in full cells with LiFePO₄ by subjecting AgFeO₂ to an extensive pre-lithiation to access such a convenient charge storage, while avoiding cyclical oxide conversion/de-conversion with associated energy losses. This full cell sustained long-term cycling retaining $\approx 80\%$ of its initial discharge capacity in complete absence of electrolyte additives with an unprecedented average energy efficiency of 88.8% and an average operational voltage of 3.0 V. These cells proved also resilient to high C-rates (up to $\approx 25C$) without undergoing major degradation and offering a good capacity retention.

Overall, these results indicate that AgFeO₂ in a nanoparticulated form is promising for the preparation of advanced LIB negative electrodes, while this appears more challenging for analogous NIB counterparts. The simplicity of its synthesis at room temperature and the possibility of reducing the Ag content in Ag_xFeO_y compositions, without compromising its outstanding electrical properties deriving from such in-situ formed Ag nanoparticles, make this iron-based compound attractive for the fabrication of environmentally friendly Li-ion cells combining robust Faradaic and pseudo-capacitive charge storage mechanisms into a single electrochemical storage device.

Acknowledgements

The authors acknowledge U. Jansson and F. Mao for help and collaboration with the project. A. Liivat and K. Edström are acknowledged for discussions and suggestions. H. Eriksson and R. Mogensen are acknowledged for valuable technical assistance. M. Valvo gratefully acknowledges the personal funding by the Swedish Research Council for Environment, Agricultural Sciences and Spatial Planning via the grant no. 245-2014-668. StandUp for Energy is also acknowledged. The Knut and Alice Wallenberg (KAW) Foundation is acknowledged for providing the electron microscopy facilities at Stockholm University.

Appendix A. Supplementary data

Supplementary data related to this article can be found at <https://doi.org/10.1016/j.jpowsour.2018.09.002>.

References

- [1] J.M. Tarascon, *ChemSusChem* 1 (2008) 777–779.
- [2] E.U. Commission, COM 297 (2014) final, (2014).
- [3] R.L. Moss, E. Tzimas, P. Willis, J. Arendorf, P. Thompson, A. Chapman, N. Morley, E. Sims, R. Bryson, J. Pearson, L. Tercero Espinoza, F. Marscheider-Weidemann, M. Soulier, A. Lüllmann, C. Sartorius, K. Ostertag, Report UR 25994 EN, (2013) <https://doi.org/10.2790/46338>.
- [4] M. Valvo, A. Liivat, H. Eriksson, C.W. Tai, K. Edström, *ChemSusChem* 10 (2017) 2431–2448.
- [5] N. Yabuuchi, K. Kubota, M. Dahbi, S. Komaba, *Chem. Rev.* 114 (2014) 11636–11682.
- [6] C. Vaalma, D. Buchholz, M. Weil, S. Passerini, *Nature Reviews Materials* 3 (2018) 18013.
- [7] W. Croft, N. Tombs, R. England, *Acta Crystallogr.* 17 (1964) 313–313.
- [8] S. Okamoto, S.I. Okamoto, T. Ito, *Acta Crystallogr. B Struct. Crystallogr. Cryst. Chem.* 28 (1972) 1774–1777.
- [9] F. Sauvage, D. Muñoz-Rojas, K. Poepfelmeier, N. Casañ-Pastor, *J. Solid State Chem.* 182 (2009) 374–380.
- [10] L. Lu, J.Z. Wang, X.B. Zhu, X.W. Gao, H.K. Liu, *J. Power Sources* 196 (2011) 7025–7029.
- [11] C.A. Cama, C.J. Pelliccione, A.B. Brady, J. Li, E.A. Stach, J. Wang, J. Wang, E.S. Takeuchi, K.J. Takeuchi, A.C. Marschilok, *Phys. Chem. Chem. Phys.* 18 (2016) 16930–16940.
- [12] A.M. Sukeshini, H. Kobayashi, M. Tabuchi, H. Kageyama, *Solid State Ionics* 128 (2000) 33–41.
- [13] X.-D. Zhu, J. Tian, S.-R. Le, J.-R. Chen, K.-N. Sun, *Mater. Lett.* 107 (2013) 147–149.
- [14] K.E. Farley, A.C. Marschilok, E.S. Takeuchi, K.J. Takeuchi, *Electrochem. Solid State Lett.* 15 (2011) A23–A27.
- [15] J.L. Durham, K. Kirshenbaum, E.S. Takeuchi, A.C. Marschilok, K.J. Takeuchi, *Chem. Commun.* 51 (2015) 5120–5123.
- [16] J.L. Durham, C.J. Pelliccione, W. Zhang, A.S. Poyraz, Z. Lin, X. Tong, F. Wang, E.S. Takeuchi, A.C. Marschilok, K.J. Takeuchi, *Applied Materials Today* 10 (2017) 142–152.
- [17] J. Durham, E.S. Takeuchi, A.C. Marschilok, K.J. Takeuchi, *ECS Transactions* 66 (2015) 111–120.
- [18] J.L. Durham, A.B. Brady, C.A. Cama, D.C. Bock, C.J. Pelliccione, Q. Zhang, M. Ge, Y.R. Li, Y. Zhang, H. Yan, *Phys. Chem. Chem. Phys.* 19 (2017) 22329–22343.
- [19] P. Poizot, S. Laruelle, S. Grugeon, L. Dupont, J.M. Tarascon, *Nature* 407 (2000) 496–499.
- [20] J. Cabana, L. Monconduit, D. Larcher, M.R. Palacín, *Adv. Mater.* 22 (2010) E170–E192.
- [21] M. Armand, J.M. Tarascon, *Nature* 451 (2008) 652–657.
- [22] J. Besenlinder, M. Hess, P. Komenda, *Solid State Ionics* 40 (1990) 525–529.
- [23] M. Obrovac, L. Christensen, D.B. Le, J.R. Dahn, *J. Electrochem. Soc.* 154 (2007) A849–A855.
- [24] M. Obrovac, V. Chevrier, *Chem. Rev.* 114 (2014) 11444–11502.
- [25] D. Bresser, S. Passerini, B. Scrosati, *Energy Environ. Sci.* 9 (2016) 3348–3367.
- [26] J.L. Durham, A.S. Poyraz, E.S. Takeuchi, A.C. Marschilok, K.J. Takeuchi, *Accounts Chem. Res.* 49 (2016) 1864–1872.
- [27] D. Zhang, Y. Li, M. Yan, Y. Jiang, *ChemElectroChem* 1 (2014) 1155–1160.
- [28] G. Taillades, J. Sarradin, *J. Power Sources* 125 (2004) 199–205.
- [29] C.-M. Park, H. Jung, H.-J. Sohn, *Electrochem. Solid State Lett.* 12 (2009) A171–A175.
- [30] I. Kovalenko, B. Zdyrko, A. Magasinski, B. Hertzberg, Z. Milicev, R. Burtovyy, I. Luzinov, G. Yushin, *Science* 334 (2011) 75–79.
- [31] R. Nagarajan, N. Tomar, *J. Solid State Chem.* 182 (2009) 1283–1290.
- [32] H. Takatsu, S. Yonezawa, S. Mouri, S. Nakatsuji, K. Tanaka, Y. Maeno, *J. Phys. Soc. Jpn.* 76 (2007) 104701.
- [33] Z. Shi, T. Wang, H. Lin, X. Wang, J. Ding, M. Shao, *Nanoscale* 5 (2013) 10029–10033.
- [34] D. Tang, G. Zhang, *Appl. Surf. Sci.* 391 (2017) 415–422.
- [35] S. Krehula, S. Mucić, *J. Mol. Struct.* 1044 (2013) 221–230.
- [36] G.I. Waterhouse, G.A. Bowmaker, J.B. Metson, *Phys. Chem. Chem. Phys.* 3 (2001) 3838–3845.
- [37] F. Mao, T. Nyberg, T. Thersleff, A.M. Andersson, U. Jansson, *Mater. Des.* 91 (2016) 132–142.
- [38] S.C. Miller, W.F. Love, *Tables of Irreducible Representations of Space Groups and Co-representations of Magnetic Space Groups*, Pruett Press, 1967.
- [39] Y. Shi, Y. Liu, H. Yang, C. Nie, R. Jin, J. Li, *Phys. Rev. B* 70 (2004) 052502.
- [40] H. Yang, Y. Xia, Y. Shi, H. Tian, R. Xiao, X. Liu, Y. Liu, J. Li, *Phys. Rev. B* 74 (2006) 094301.
- [41] M. Iliev, A. Litvinchuk, R. Meng, Y. Sun, J. Cmaidalka, C. Chu, *Phys. C Supercond.* 402 (2004) 239–242.
- [42] D. De Faria, S. Venâncio Silva, M. De Oliveira, *J. Raman Spectrosc.* 28 (1997) 873–878.
- [43] S.J. Oh, D. Cook, H. Townsend, *Hyperfine Interactions* 112 (1998) 59–66.
- [44] J. Kugbe, N. Matsue, T. Henmi, *J. Hazard Mater.* 164 (2009) 929–935.
- [45] R. Pozas, M. Ocaña, M.P. Morales, C.J. Serna, *J. Colloid Interface Sci.* 254 (2002) 87–94.
- [46] M. Valvo, F. Lindgren, U. Lafont, F. Björefors, K. Edström, *J. Power Sources* 245 (2014) 967–978.
- [47] W.J. Plieth, *J. Phys. Chem.* 86 (1982) 3166–3170.
- [48] P.L. Redmond, A.J. Hallock, L.E. Brus, *Nano Lett.* 5 (2005) 131–135.
- [49] R.A. Masitas, F.P. Zamborini, *J. Am. Chem. Soc.* 134 (2012) 5014–5017.
- [50] J. Morales, L. Sánchez, F. Martín, J. Ramos-Barrado, M. Sánchez, 203rd ECS meeting - Paris, meeting abstracts, *Absatzwirtschaft* 118 (2003).
- [51] J. Morales, L. Sánchez, F. Martín, J. Ramos-Barrado, M. Sánchez, *J. Electrochem. Soc.* 151 (2004) A151–A157.
- [52] M. Wachtler, M. Winter, J.O. Besenhard, *J. Power Sources* 105 (2002) 151–160.
- [53] S. Laruelle, S. Grugeon, P. Poizot, M. Dollé, L. Dupont, J.M. Tarascon, *J. Electrochem. Soc.* 149 (2002) A627–A634.
- [54] P. Balaya, A.J. Bhattacharyya, J. Jamnik, Y.F. Zhukovskii, E.A. Kotomin, J. Maier, *J. Power Sources* 159 (2006) 171–178.
- [55] J. Maier, *Nat. Mater.* 4 (2005) 805–815.
- [56] J. Maier, *J. Power Sources* 174 (2007) 569–574.
- [57] J. Morales, L. Sánchez, F. Martín, F. Berry, X. Ren, *J. Electrochem. Soc.* 152 (2005) A1748–A1754.
- [58] A.C. Marschilok, E.S. Kozarsky, K. Tanzil, S. Zhu, K.J. Takeuchi, E.S. Takeuchi, *J. Power Sources* 195 (2010) 6839–6846.
- [59] S. Grugeon, S. Laruelle, R. Herrera-Urbina, L. Dupont, P. Poizot, J.M. Tarascon, *J. Electrochem. Soc.* 148 (2001) A285–A292.
- [60] E. García-Tamayo, M. Valvo, U. Lafont, C. Locati, D. Munao, E.M. Kelder, *J. Power Sources* 196 (2011) 6425–6432.
- [61] M. Valvo, E. García-Tamayo, U. Lafont, E.M. Kelder, *J. Power Sources* 196 (2011) 10191–10200.
- [62] Y.Z. Jiang, D. Zhang, Y. Li, T.Z. Yuan, N. Bahlawane, C. Liang, W.P. Sun, Y.H. Lu, M. Yan, *Nanomater. Energy* 4 (2014) 23–30.
- [63] S. Nordlinder, L. Nyholm, T. Gustafsson, K. Edström, *Chem. Mater.* 18 (2006) 495–503.
- [64] M. Valvo, B. Philippe, F. Lindgren, C.W. Tai, K. Edström, *Electrochim. Acta* 194 (2016) 74–83.
- [65] P. Balaya, H. Li, L. Kienle, J. Maier, *Adv. Funct. Mater.* 13 (2003) 621–625.
- [66] J. Jamnik, J. Maier, *Phys. Chem. Chem. Phys.* 5 (2003) 5215–5220.
- [67] B. Philippe, M. Valvo, F. Lindgren, H. Rensmo, K. Edström, *Chem. Mater.* 26 (2014) 5028–5041.
- [68] B. Huang, K. Tai, M. Zhang, Y. Xiao, S.J. Dillon, *Electrochim. Acta* 118 (2014) 143–149.
- [69] W.E. Freeth, G.V. Raynor, *J. Inst. Met.* 82 (1953) 569–574.
- [70] A. Pelton, *Bulletin of Alloy phase diagrams* 7 (1986) 223–228.
- [71] A. Pelton, *Bulletin of Alloy Phase Diagrams* 7 (1986) 133–136.
- [72] G. Kienast, J. Verma, W. Klemm, *Z. Anorg. Allg. Chem.* 310 (1961) 143–169.
- [73] D.I. Iermakova, R. Dugas, M.R. Palacín, A. Ponrouch, *J. Electrochem. Soc.* 162 (2015) A7060–A7066.
- [74] M.Á. Muñoz-Márquez, D. Saurel, J.L. Gómez-Cámer, M. Casas-Cabanas, E. Castillo-Martínez, T. Rojo, *Advanced Energy Materials* 7 (2017) 1700463.
- [75] A. Varzi, D. Bresser, J. von Zamory, F. Muller, S. Passerini, *Advanced Energy Materials* 4 (2014) 1400054.
- [76] D. Bresser, E. Paillard, R. Kloepsch, S. Krueger, M. Fiedler, R. Schmitz, D. Baitner, M. Winter, S. Passerini, *Advanced Energy Materials* 3 (2013) 513–523.
- [77] J. Hassoun, F. Croce, I. Hong, B. Scrosati, *Electrochem. Commun.* 13 (2011) 228–231.
- [78] R.D. Shannon, D.B. Rogers, C.T. Prewitt, J.L. Gillson, *Inorg. Chem.* 10 (1971) 723–727.
- [79] M.A. Marquardt, N.A. Ashmore, D.P. Cann, *Thin Solid Films* 496 (2006) 146–156.
- [80] X. Lou, X. Wu, Y. Zhang, *Electrochem. Commun.* 11 (2009) 1696–1699.